Research Article

Applying Energy-Dispersive X-Ray Fluorescence Analysis to Detect Tungsten Inclusions in Nuclear Fuel Rod End Plug TIG Welds

Runqiu Gu, Jianfeng Cheng, Wanchang Lai [ID], and Guangxi Wang

College of Nuclear Technology and Automation Engineering, Chengdu University of Technology, Chengdu 610059, China

Correspondence should be addressed to Wanchang Lai; lwchang@cdut.edu.cn

This study proposes a new method of detecting tungsten inclusions in nuclear fuel rod upper-end plug welds using energy-dispersive X-ray fluorescence (EDXRF) analysis. The Monte Carlo simulation method was used to simulate the process of detecting tungsten inclusions in nuclear fuel rod upper-end plug welds by the EDXRF. The detectable tungsten particle diameters in the zirconium alloy at different depths in welds and the detection limits of the trace tungsten dispersed in welds were obtained. Then, we constructed an experimental device that uses a CdTe detector with an X-ray tube. The results showed that the relative standard deviation of the net count rate of tungsten K-series characteristic X-rays $[W(K_\alpha)]$ was 1.46%, and the optimum parameters are a tube voltage of 150 kV and current of 0.5 mA. These values were used to perform energy-dispersive X-ray fluorescence analysis. These results were compared to the X-ray radiographic results, which were broadly similar. Furthermore, the results of EDXRF analysis were more legible and reliable than those from X-ray radiographic inspections. This study demonstrates the feasibility of applying EDXRF analysis to detect tungsten inclusions.

1. Introduction

Most nuclear fuel rods contain an upper-end plug, a cladding tube, fuel pellets, and a lower-end plug [1, 2]. To prevent radioactive fission products from leaking during the fuel rod manufacturing process, sealed welds are required between the fuel cladding tube and end plug. End plug welding is the most crucial procedure during nuclear fuel rod manufacturing [3–5]. Tungsten inert gas welding (TIG) produces relatively strong and higher quality welds, so it is widely used to weld precision instruments in the atomic energy and aviation industries [6–9]. If they are not inspected during welding, these welds can contain many types of defects. Under stress, these defects may grow and lead to failure.

Tungsten inclusions are one type of welding defect. They are formed when the end plug and cladding tube of nuclear fuel rods are welded using the TIG method. The tungsten electrode can break and fall into the welded pool because of the wrong polarity of the power source or a high current density. The geometric shape of the tungsten inclusions is irregular, and its sharp corners have a splitting effect on the weld. This inclusion easily produces stress concentrations and microcracks and reduces the toughness and strength of the weld [10].

An inclusion defect can reduce the strength and toughness of the end plug welds. This defect results in a decline in the quality of end plug welds and reduces the nuclear fuel rod's life. When nuclear fuel rods are exposed to the severe conditions of high temperature, high pressure, and intense radiation for an extended period of time, any existing weld defects are likely to be further expanded. As a result, radioactive fission products can escape through the defects and damage the reactor cooling circuit. In severe cases, it will cause damage to the fuel rod cladding, which affects the safe operation of the nuclear reactor and can cause substantial economic losses [11, 12]. Therefore, it is essential to detect these tungsten inclusion defects in the welding process.

Metallographic examination and X-ray radiography are commonly used methods of detecting these defects. However, metallographic inspection damages the sample and

cannot test every fuel rod in the production process. This method is more suitable for the analysis and testing of spent fuel. Although the X-ray imaging detection method can be used to detect tungsten inclusion defects, the size that can be seen is limited [13, 14]. A study by Hui et al. showed that a cylindrical girth weld's image sensitivity (minimum visible wire diameter) is 0.20 mm in digital X-ray radiography, and the end girth weld is 0.10 mm [15]. In a study by Ewert et al. an X-ray digital imaging detection method was used to examine the welds in the austenite pipelines of nuclear power plants. Some cracks and pores (approximately 0.2 mm) were detected [16]. When using TIG to weld, the broken tungsten electrodes may be melted in the molten pool of the end plug, or they may exist in the form of particles. When a small amount of tungsten is present in the weld seam of an end plug, it is even more challenging to accurately identify it by X-ray imaging. In addition, the results are greatly influenced by human factors, and therefore, the reliability is low. Although the above methods can detect tungsten inclusions, each has disadvantages.

This article uses EDXRF to detect whether tungsten is in the weld and identify any tungsten inclusions. EDXRF analysis is an analytical method used to determine the type and content of elements in a material. It uses primary X-ray photons to excite atoms to generate secondary characteristic X-rays. A detector characterizes the photons with a pulse height analyzer for element identification according to the spectrum for a pulse height distribution, which can then be used for the quantitative analysis of elements. The analysis time depends on the type of instrument, which varies from tens of seconds to several minutes. This method can analyze more than 80 elements between Be and U. Its sensitivity is broad, as it can explore from ppm to 100%. The EDXRF method has many advantages: it is fast, easy to operate, nondestructive, and provides in situ analysis [17–21]. As a result, it has been used for decades in archaeology, geology, biology, chemistry, and other fields [22–31]. In this paper, we use EDXRF to detect tungsten inclusions in the welds of nuclear rods.

2. Methods and Experimental

2.1. MCNP Simulation. It is common to simulate EDXRF through Monte Carlo software. This paper uses a MCNP5 Monte Carlo simulation software package to do so. This simulation includes two items. The first is to simulate the diameter of tungsten particles that can be identified at different depths of zirconium alloys. The second is to simulate the detection limit of tungsten when tungsten inclusions melt on the top of the end plug.

Figure 1 shows a diagram of the detection device that was used in the Monte Carlo simulation. The detector is a CdTe detector (Amptek, X-123) which uses the parameters shown in Table 1. In the simulation, the sensor was simplified to include only the CdTe sensitive volume, the Be window, and the top shell of the detector. This simulation uses the device's dimensions and the parameters described later in the paper. The X-ray source uses a 150 KV rhodium spectrum. The MCNP5 results are normalized for each particle. The photon
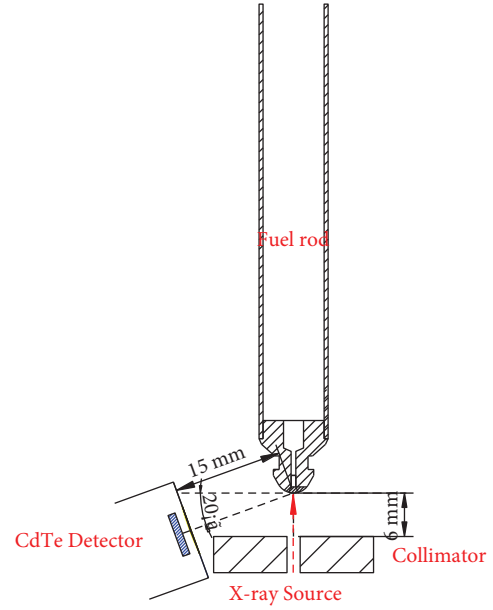

Figure 1: Schematic diagram of the detection device in the Monte Carlo simulation.

Table 1: Main parameters of CdTe detector.

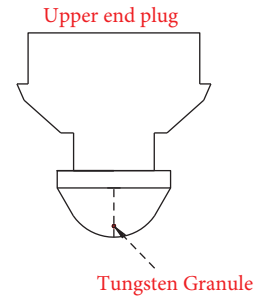| Technical index	Parameters
Detector type	Cadmium telluride (CdTe) diode
Detector area	$9\,mm^2$
Detector thickness	1 mm
Detector window	Be: 4 mm thick $(100\,\mu m)$
Resolution	<1.2 keV FWHM@122 keV, typical
Maximum count rate	Up to 2×10^5 cps
Optimal energy range	5 to 150 keV

Figure 2: Schematic diagram of simulation experiment for tungsten particle detection.

is counted by the F1 card, which bins the data into energy intervals. The photon energy is recorded at intervals of 0.1 keV from the minimum energy of 1 keV to the maximum energy. The number of photons is counted by the energy box method, similar to that used to determine the multichannel spectral statistics. The simulation includes the interactions of electrons and photons. We used the default setting of the PHYS card, which used a detailed physical simulation of the MCNP, which used the photoelectric effect, Thomson coherent scattering, Compton scattering, and pair production.

The number of simulated particles was 2×10^9. It took approximately eight hours for each program to perform the calculations.

Figure 2 is a schematic diagram of the simulation. The depth of the zirconium alloy was 0 mm to 0.7 mm with a 0.1 mm step size. The diameter of tungsten particles varied from 0.01 mm to 0.5 mm. Particles were placed in the center of the shaft to simplify the model. The weld seam was approximately hemispherical (the nuclear fuel rod can be rotated for multiple measurements). When simulating each depth, the tungsten particles were located at the farthest distance from the detector. When the particles are farther from the axis, the signal increases and the identifiable size of the particles become smaller. Figure 3 is a diagram of the simulation when the tungsten inclusions are present in the upper-end plug weld in a dispersed form after melting. In the simulation, tungsten elements were only added to the upper-end plug welding and the content distributed in a range of approximately 50–800 ppm.

2.2. Experimental Apparatus.

The X-ray energy device consists of a CdTe detector (Amptek, X-123 model) and an X-ray tube (BJKVXD, Series X160k1mA-B). The CdTe detector and X-ray tube parameters are shown in Tables 1 and 2, respectively. A schematic diagram of the device is presented in Figure 4. The angle between the detector centerline and horizontal line was 20°. The distance from the collimator outlet to the welds was 6 mm, and the distance from the detector outlet to the end plug welding point was 15 mm. The X-123 CdTe was a completely integrated system that contained a CdTe detector, a preamplifier, a DP5 digital pulse processor (DPP) and MCA, and a PC5 power supply. The X-ray tube was equipped with a power supply and control software. The CdTe detector and X-ray tube were independent of each other. We used the X-ray tube's primary rays to excite tungsten X-rays in the welds. We used the sensor to measure the excited X-rays. The experimental data were collected and analyzed by the MCA and DPPMCA software with X-123 CdTe.

2.3. Samples.

The experimental samples were obtained from the Nuclear Fuel Element Manufacturing Company as shown in Figure 5. There were seven nuclear fuel rods in group A and ten in group B. A schematic diagram of the nuclear fuel rods is shown in Figure 6. All the samples included a part of the fuel cladding tube and upper-end plug. The upper-end plug, cladding tube, and hole in the upper-end plug were welded together via TIG. The sealing welds on the upper-end plug were measured. X-ray energy spectrum analysis was used to detect whether tungsten inclusions were in the nuclear fuel rod upper-end plug welds. The analytical results were compared with radiography images provided by the Nuclear Fuel Element Manufacturing Company.

2.4. Experiments.

To evaluate the device's precision, the No. 7 nuclear fuel rod from group A was used in an experiment. The net area and value of the peak position of $W (K_\alpha)$ were
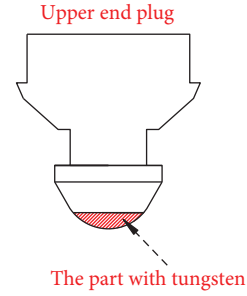

FIGURE 3: Schematic diagram of simulation experiment for detecting dispersed tungsten.

TABLE 2: Parameters of the X-ray tube.

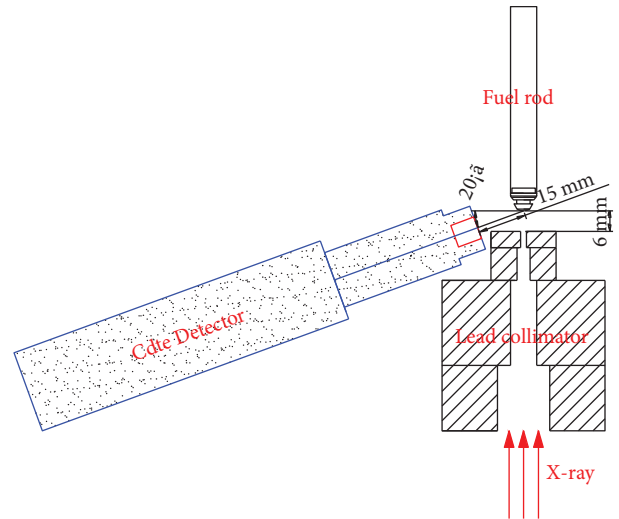| Anode	Focus size	Tube voltage	Anode current
Rhodium	0.8 * 0.8 mm	130 to 160 kV	0.3 to 1.0 mA

FIGURE 4: Diagram of the experimental device.

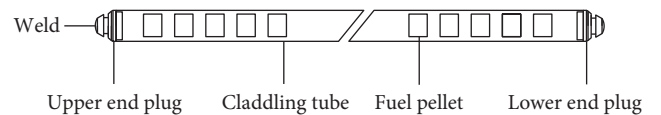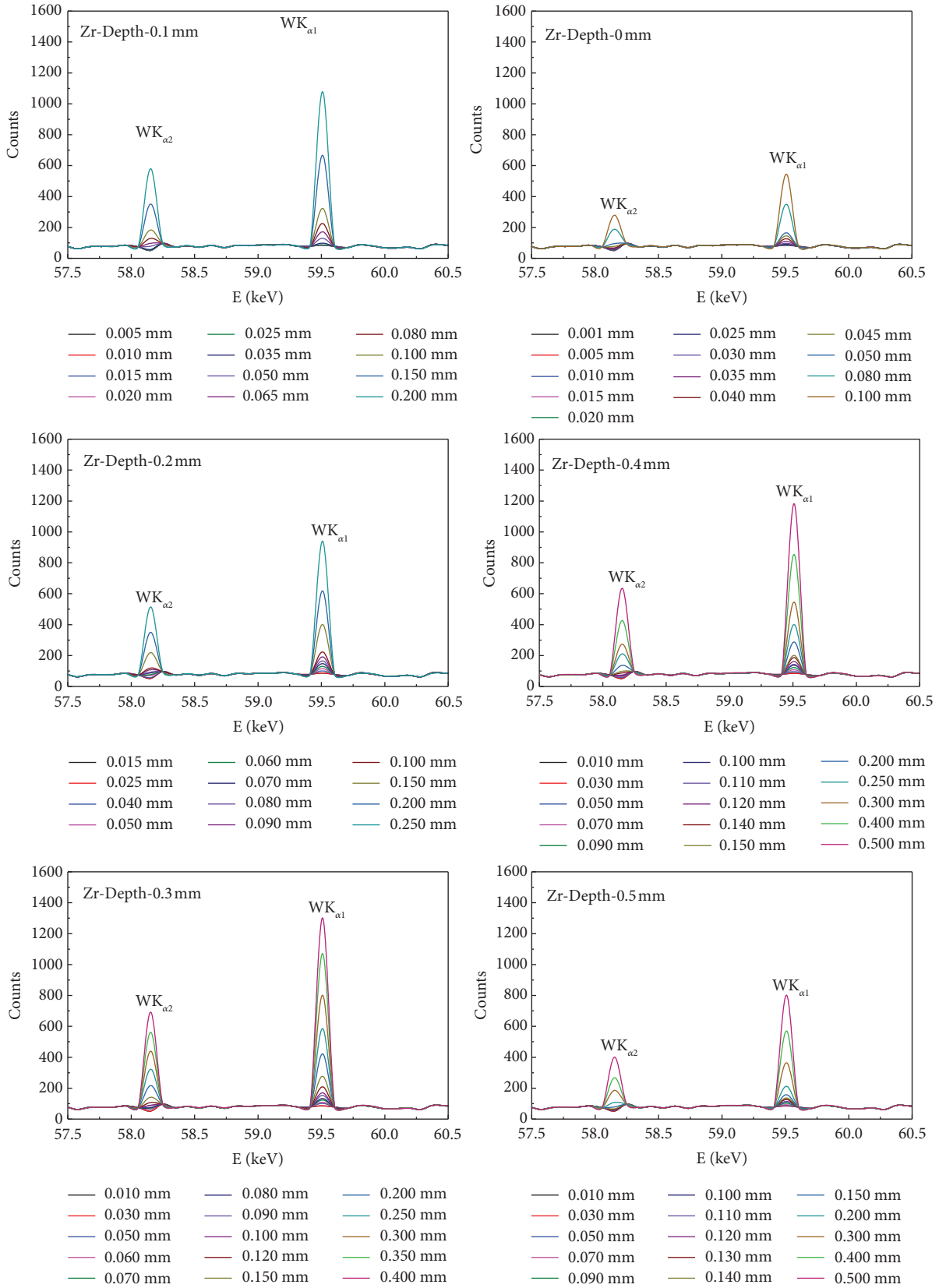FIGURE 5: Experimental samples.

FIGURE 6: Schematic diagram of the nuclear fuel rod structure.
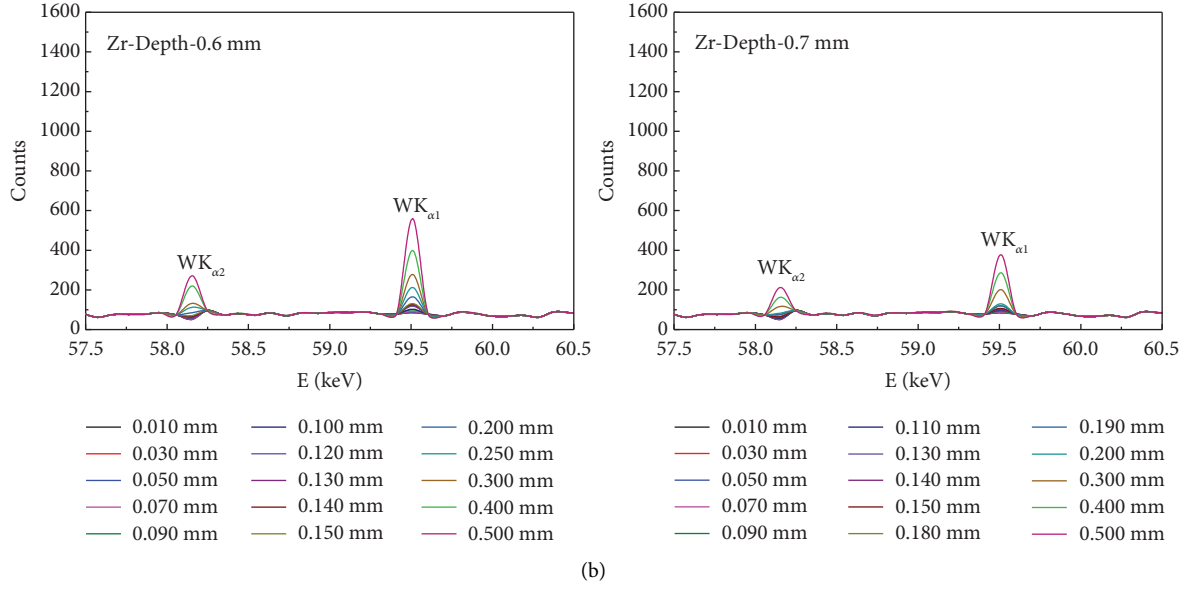
(a)

Figure 7: Continued.

(b)

FIGURE 7: The simulation of tungsten particles at different zirconium depths.

used as an index to evaluate the device's precision. Next, we optimized tube voltage and anode current, and the net count rate and the peak-to-background ratio of the $W (K_\alpha)$ were used as evaluation indicators.

The tube voltage setting range was from 130 kV to 160 kV with an interval of 10 kV. The anode current varied from 0.3 mA to 0.9 mA with an interval of 0.1 mA. Each measured condition was valuated at least five times with no changes in the other parameters. The tube voltage and anode current were combined to produce 28 measurements. Using these optimal parameters, we took an EDXRF analysis of the nuclear fuel rods and compared the results with X-ray radiography measurements.

3. Results and Discussion

3.1. Monte Carlo Simulation Results. Monte Carlo simulation method is used to simulate the identifiable diameter of tungsten particles at different depths in the zirconium alloy in the rod. Figure 7 shows the energy spectrum from the simulation.

In the manufacturing of nuclear fuel rods, the effective penetration depth of the end plug is required to be less than or equal to 0.65 mm. Our Monte Carlo simulation studies the depths of approximately 0–0.7 mm. It can be seen from Figure 7 that the W characteristic X-ray intensity of different diameters tungsten particles is various at different depths of the zirconium alloy. According to the formula [32, 33], the detection limit of the W peak can be calculated. The results are shown in Table 3. We fit these results and obtained a function of the depth of the zirconium alloy with the diameter of the tungsten particles. The results are shown in Figure 8.

It can be seen from Table 3 and Figure 8 that, as the depth of the zirconium alloy increases, the size of the identifiable particles also increases. The depth of the zirconium alloy has

TABLE 3: Results of the simulation.

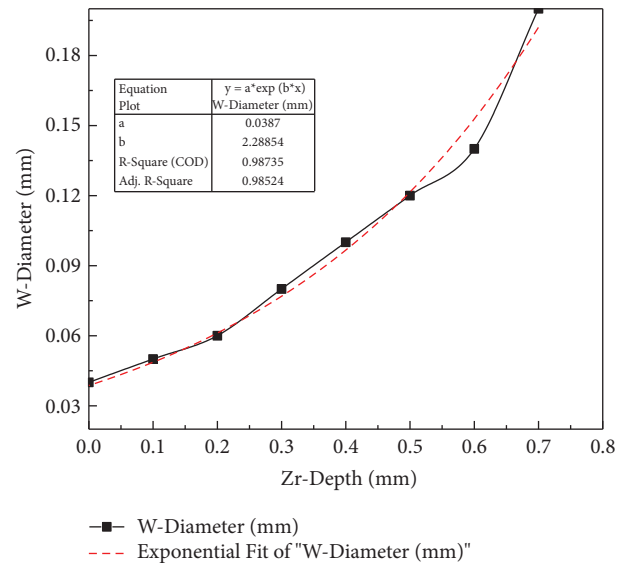| Zr depth (mm)	W diameter(mm)
0	0.04
0.1	0.05
0.2	0.06
0.3	0.08
0.4	0.10
0.5	0.12
0.6	0.14
0.7	0.20

FIGURE 8: Fitted graph of zirconium alloy depth and detectable tungsten particle diameter.
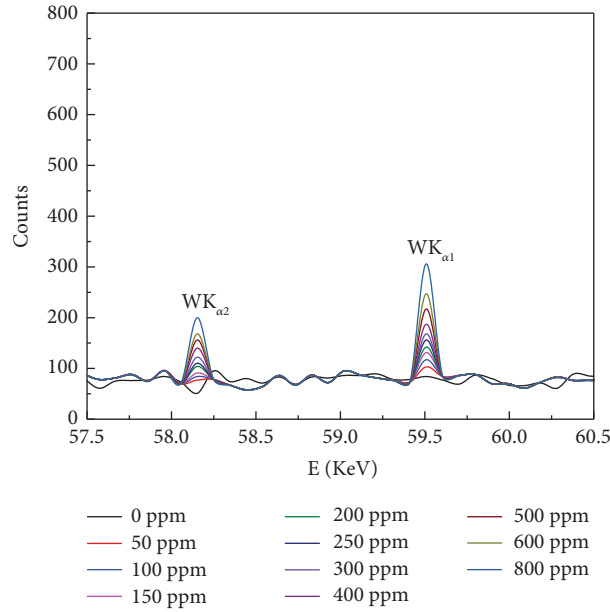
Figure 9: Energy spectrum of the simulation results of different tungsten contents in the end plug welds.

Table 4: Peak area counts of the simulation of different contents of tungsten in end plug welds.

Content (ppm)	LOD	50.0	100	150	200	250	300	400	500	600	800
Net peak counts	26.8	21.9	35.9	50.0	61.0	75.0	87.0	106	136	166	225

an exponential relationship with the size of the identifiable tungsten particles.

Tungsten inclusions are not allowed in the manufacturing process of nuclear fuel rods. However, in the existing technology, the size of detectable tungsten is limited. Research by Hui et al. showed that the X-ray imaging method could effectively detect pores, inclusions, and other defects with a diameter greater than 0.2 mm in the cylindrical girth weld of the annular nuclear fuel element. The device can see volumetric flaws such as pores and inclusions. At the end of the rod, it can detect face girth welds with a diameter greater than 0.1 mm. By comparison, EDXRF can detect smaller defects in the range of approximately 0–0.4 mm.

As shown in Figure 3, we simulated adding evenly dispersed trace tungsten in the range of 50 ppm to 800 ppm, alongside blank samples. The results are shown in Figure 9, and the calculated values and detection limit are shown in Table 4.

It can be seen from Table 4 that the detection limit of tungsten is about 100 ppm. From the previous analysis, there is a certain size limit for the detection of tungsten in welds from X-ray radiography. When tungsten is melted into the weld, it is challenging to detect it by X-photographic methods. Under certain conditions, the EDXRF method can detect tungsten inclusions in the weld tungsten. In the production of nuclear fuel rods, tungsten inclusions are not allowed in the end plug welds. The simulation shows that the detection of these inclusions is better with EDXRF than X-ray radiography because it can detect inclusions that are smaller in size and content.

3.2. Determining the Device's Precision. To evaluate the device's precision, the No. 7 fuel rod in group A was placed on the measurement device, and the noncontinuous repeated measurement was performed at least 20 times. The measurement time was 60 s, the X-ray tube voltage was 160 kV, and the anode current was 0.6 mA. The individual results were reported, and the average net count rate, average deviation (AD), relative average deviation (RAD), standard deviation (SD), and relative standard deviation (RSD) were calculated.

Figure 4 shows the measured value of the W (K_α) net count rate and deviation. Table 3 presents the average net count rate, average deviation, relative average deviation, standard deviation, and relative standard deviation of the net count rate of the W (K_α).

As shown in Figure 10 and Table 5, the average net count rate of W (K_α) was 68.2, and the deviation range was from −1.51 to 1.6. The W (K_α) peak position's channel was almost at the same location each time (channel 1354), and only three measurement results slightly differed. Table 3 shows that the relative standard deviation of W (K_α)'s net count rate was 1.46%. The data from each test had no significant differences. The results demonstrate that the X-ray analysis was precise and provided accurate data.

3.3. Tube Voltage and Anode Current. In X-ray energy spectrum analysis, the sample's characteristic element X-ray is excited by the X-ray tube's primary spectrum. If the X-ray tube's voltage is too low, the primary spectrum's energy will
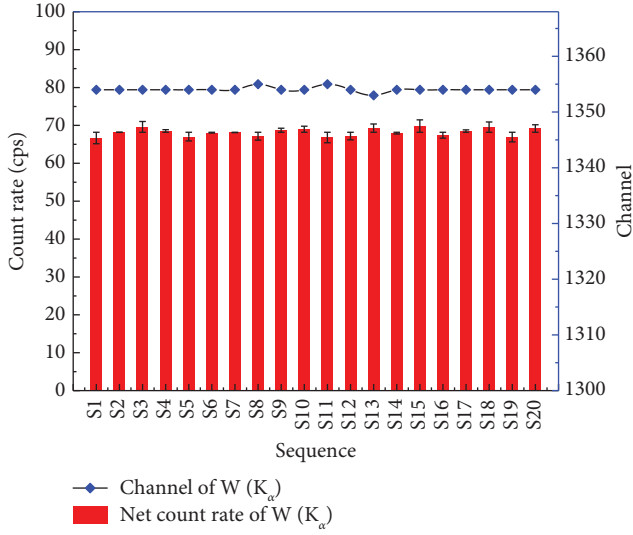
FIGURE 10: Results of the precision experiments. The error bars represent the difference between the measurement and the average.

FIGURE 11: Net count rate of the $W (K_\alpha)$ under different tube voltages and currents.

TABLE 5: Parameters of measurement results.

AVG	AD	RAD (%)	SD	RSD (%)
68.2	0.851	1.25	0.995	1.46

not reach the characteristic element X-ray's absorption edge. If it is too high, a more significant bremsstrahlung background is introduced, and the measurement results will be affected. Changing the X-ray tube's current will have an impact on the measurement's signal-to-noise ratio. Therefore, detecting tungsten inclusions requires a suitable tube voltage and current. Because of those reasons, we varied the tube voltage and current. Figures 11 and 12 present the results.

As shown in Figure 11, the net count rate of the $W (K_\alpha)$ had a constant upward trend as the tube voltage and current increased. However, the $W (K_\alpha)$ peak-to-background of the trend was different as the tube voltage and current changed. Figure 12 demonstrates that the peak-to-background ratio of the $W (K_\alpha)$ steadily increases as the X-ray tube voltage increases at the same tube current. The peak appeared when the tube voltage was approximately 150 kV and then decreased slightly. As the tube current increased, the peak-to-background ratio of the $W (K_\alpha)$ first showed an upward trend and then slowly became smaller. When the tube voltage was in the range of approximately 130 kV–140 kV, the peak-to-background ratio of $W (K_\alpha)$ had the maximum value at a tube current of 0.5 mA, and when the voltage was 150 kV~160 kV, the peak-to-background ratio of $W (K_\alpha)$ had a higher value at a wide range of tube currents from 0.4 mA to 0.6 mA. In general, when the X-ray tube voltage was 150 kV and the current was 0.5 mA, the peak-to-background ratio of $W (K_\alpha)$ had a relatively high value, and the net count rate of $W (K_\alpha)$ was also greater than 70. According to the results, we selected 150 kV and 0.5 mA as the X-ray tube's operating parameters for the following experiments.
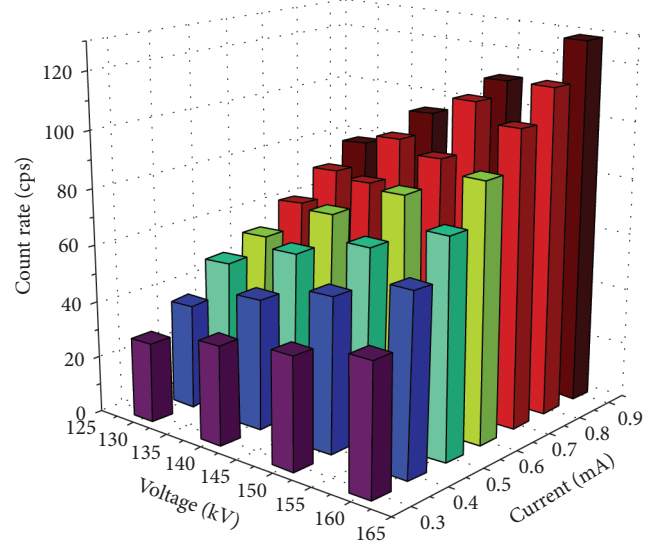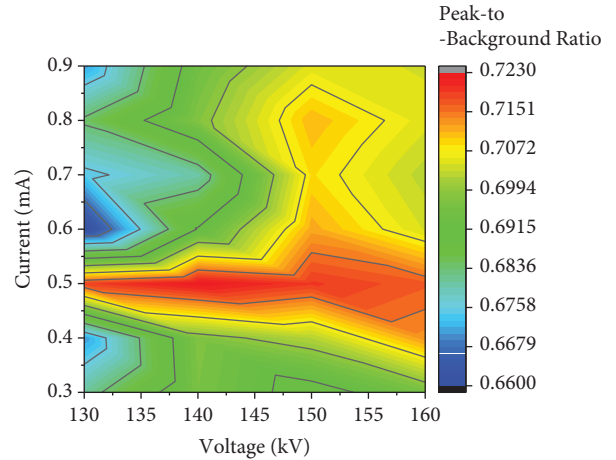

FIGURE 12: Peak-to-background of the $W (K_\alpha)$ under different tube voltages and currents.

3.4. Detection of Tungsten Inclusions. Using these experiments, we obtained the optimal conditions for analyzing tungsten inclusions using EDXRF analysis. We used X-ray energy spectrum analysis to test two batches of samples from the Nuclear Fuel Element Manufacturing Company. The measurement results are shown in Figures 13 and 14.

Figure 13 shows the X-ray energy spectra of the nuclear fuel rods in group A. The chart indicates that there were no obvious characteristic X-ray peaks in fuel rods No. 1 to No. 6. However, there were obvious characteristic X-ray peaks of tungsten element in the X-ray energy spectrum of fuel rod No. 7, where the peaks of $W (K_{\alpha 1})$, $W (K_{\alpha 2})$, $W (K_{\beta 1})$, and $W (K_{\beta 2})$ are visible. The results demonstrated that there were tungsten inclusions in that rod.

Figure 15 presents a radiography image of the nuclear fuel rods in group A from the Nuclear Fuel Element Manufacturing Company. As shown in the radiography
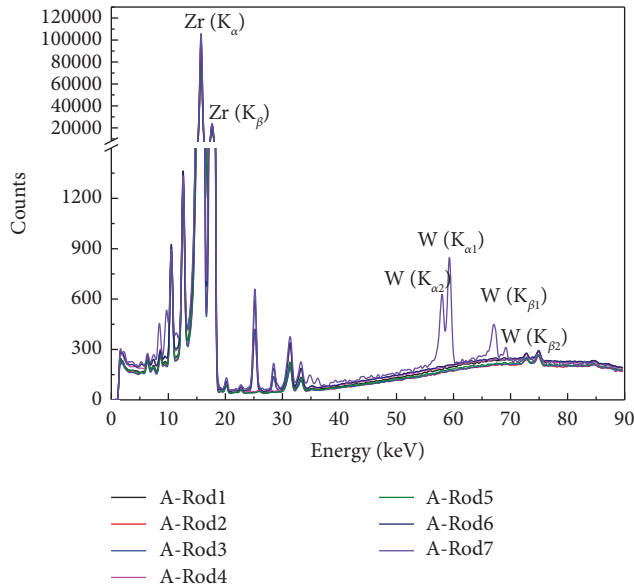
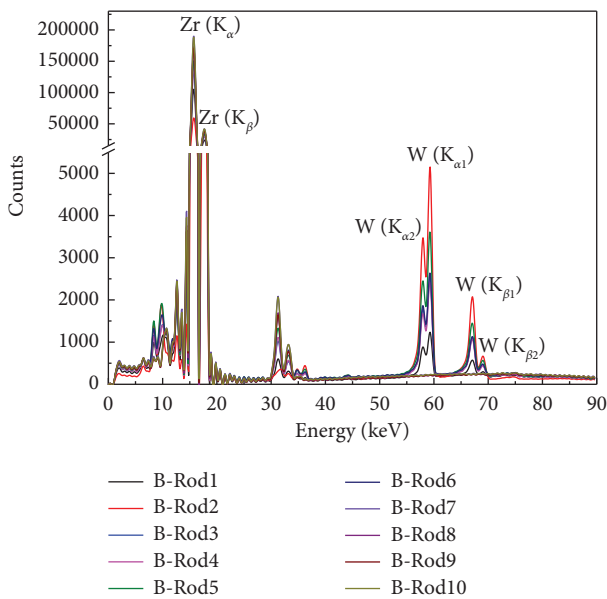FIGURE 13: X-ray energy spectra of the nuclear fuel rods in group A.

FIGURE 14: X-ray energy spectra of the nuclear fuel rods in group B.

FIGURE 15: Radiography image of the nuclear fuel rods in group A.

FIGURE 16: Radiography image of nuclear fuel rods in group B.

image, there was a white area in the upper end plug welds (the area circled by the red box). The Nuclear Fuel Element Manufacturing Company staff concluded that the white area's position is the area containing tungsten inclusions. Tungsten inclusions appeared because during the inert tungsten gas-shielded welding process, high-density tungsten from the electrode tip was trapped and deposited in the weld. There was no white area in the radiography images of fuel rods No. 1 to No. 6, which indicated that these fuel rods had no tungsten inclusions. Comparing the energy-dispersive X fluorescence analysis results with the radiography imaging results demonstrated that the two methods agree.

Figure 14 shows the X-ray energy spectra of group B nuclear fuel rods, and Figure 16 presents a radiography image of group B. The group B spectra demonstrated that fuel rods No. 1 to No. 6 had characteristic X-ray peaks of tungsten, but fuel rods No. 7 to No. 10 did not. The radiography images showed that fuel rods No. 1 to No. 6 had a white area in the upper-end plug welds (the area circled by the red box), indicating that these fuel rods had tungsten inclusions in the nuclear fuel rod upper-end plug welds. In the group B fuel rods, the two methods of detecting tungsten inclusions were consistent.

Comparing the EDXRF results and X-ray radiographic results, it can be seen that some of the X-ray radiographic inspection results are not very clear. These results require professional inspectors who have years of work experience to determine whether there are tungsten inclusions. However, the results from EDXRF analysis are clearly evident.

4. Conclusions

Detecting tungsten inclusions in nuclear fuel rod upper-end plug welds is an indispensable and vital step in the manufacturing process of nuclear fuel assemblies. This step is critical to ensure the safe operation of nuclear reactors. The main disadvantages of current methods are destructiveness, complicated procedures, lack of real-time data, and the limited size and content of detectable inclusions. This paper uses Monte Carlo software to simulate the EDXRF analysis of tungsten inclusions in nuclear fuel rods. The results show that the EDXRF analysis method is superior to the X-ray radiography method, as it can detect welds at the depth range of 0 to 0.4 mm. In addition, this paper also simulates the trace tungsten inclusions dispersed in the weld. The results show that the detection limit of EDXRF can reach 100 ppm. However, when tungsten inclusions are present, it is challenging to detect them by X-ray radiography. EDXRF analysis was carried out on the solder joints of the upper-end plugs of two sets of nuclear fuel rods using a measuring device. The results were consistent with X-ray inspections, but the EDXRF analysis had better readability and reliability. EDXRF does not damage the nuclear fuel rods and improves the reliability of detecting tungsten in the nuclear fuel

manufacturing process. Therefore, this method can achieve real-time quality control of nuclear fuel rod welds.

Data Availability

The data used to support the findings of this study are included within the article.

Conflicts of Interest

The authors declare that there are no conflicts of interest regarding the publication of this paper.

Acknowledgments

References

[1] G. Ferrari, G. Franchini, P. Balasubramanian et al., "Nonlinear vibrations of a nuclear fuel rod supported by spacer grids," *Nuclear Engineering and Design*, vol. 361, Article ID 110503, 2020.

[2] V. Zeman and Z. Hlavá, "Prediction of the nuclear fuel rod abrasion in the probability sense," *Applied Mechanics and Materials*, vol. 821, pp. 317–324, 2013.

[3] K. T. Bates, "Resistance welding of zircaloy end closure joints," in *Proceedings of the Nuclear Industry Fair and Technical Meetings*, Basel, Switzerland, 1966.

[4] L. E. Mills, "Zircaloy welding techniques developed for plutonium recycle program UO₂ fuel element fabrication," *Welding Journal*, vol. 40, 1961.

[5] L. T. Babkin, K. K. Sukhov, D. V. Sannikov, A. Y. Yashunskii, and O. K. Peslyak, "Sealing of fuel elements for nuclear reactors by resistance butt welding," *Welding International*, vol. 14, no. 2, pp. 162–164, 2000.

[6] J. W. Lee, J. H. Kim, K. H. Kim, J. Y. Park, and S. H. Kim, "Development of end plug welding technique for SFR fuel rod fabrication," *Science and Technology of Nuclear Installations*, vol. 2016, Article ID 9549805, 9 pages, 2016.

[7] M. C. Liu, F. Q. Chen, X. X. Si, and B. Wang, "The sealing welding of helium-filled hole on nuclear fuel rod," *Applied Mechanics and Materials*, vol. 217–219, pp. 2070–2074, 2012.

[8] R. G. Shanmuga, R. B. Venkat, and R. A. John, "A six sigma frame work for reduction of GTAW weld defect tungsten inclusion in a nuclear piping facility," *National Journal on Advances in Computing & Management*, vol. 5, pp. 15–20, 2014.

[9] A. Pai, I. Sogalad, S. Basavarajappa, and P. Kumar, "Assessment of impact strength of welds produced by cold wire and hot wire gas tungsten arc welding (GTAW) processes," *Materials Today: Proceedings*, vol. 24, pp. 983–994, 2020.

[10] N. M. Nandhitha, N. Manoharan, B. S. Rani, B. Venkataraman, P. K. Sundaram, and B. Raj, "Detection and quantification of tungsten inclusion in weld thermographs for on-line weld monitoring by region growing and morphological image processing algorithms," in *Proceedings of the International Conference on Computational Intelligence and Multimedia Applications (ICCIMA 2007)*, pp. 513–518, IEEE, Sivakasi, India, December 2007.

[11] B. B. Lahiri, S. Bagavathiappan, T. Saravanan et al., "Defect Detection in Weld Joints by Infrared Thermography," in *Proceedings of the International Conference on Non Destructive Evaluation in Steel and Allied Industries*, Indira Gandhi Centre for Atomic Research, Jamshedpur, India, December 2011.

[12] T.-H. Na, B.-H. Lee, M.-W. Kim et al., "Quality monitoring of end plug resistance weldment for nuclear fuel rods by electrode displacement," *International Journal of Advanced Manufacturing Technology*, vol. 99, no. 9–12, pp. 2509–2522, 2018.

[13] B. Çevik, "Gas tungsten arc welding of 7075 aluminum alloy: microstructure properties, impact strength, and weld defects," *Materials Research Express*, vol. 5, p. 66540, 2018.

[14] T. Saravanan, S. Bagavathiappan, J. Philip, T. Jayakumar, and B. Raj, "Segmentation of defects from radiography images by the histogram concavity threshold method," *Insight - Non-Destructive Testing and Condition Monitoring*, vol. 49, no. 10, pp. 578–584, 2007.

[15] T. Hui, Z. Xiaogang, and Y. Dongbao, "Digital X-ray imaging inspection of annular nuclear ful element weld," *Nondestructive Testing*, vol. 43, pp. 83–86, 2021.

[16] U. Ewert, B. Redmer, D. Walter et al., "X-ray tomographic in-service inspection of girth welds—the European project TomoWELD," in *Proceedings of the 41st Annual Review of Progress in Quantitative Nondestructive Evaluation*, vol. 1650, pp. 525–533, Boise, ID, USA, 2015.

[17] B. Kanngießer, I. Mantouvalou, W. Malzer, T. Wolff, and O. Hahn, "Non-destructive, depth resolved investigation of corrosion layers of historical glass objects by 3D micro X-ray fluorescence analysis the HTML version of this article has been enhanced with colour images," *Journal of Analytical Atomic Spectrometry*, vol. 23, pp. 814–819, 2008.

[18] P. J. Potts, P. C. Webb, and J. S. Watson, "Energy-dispersive x-ray fluorescence analysis of silicate rocks for major and trace elements," *X-Ray Spectrometry*, vol. 13, no. 1, pp. 2–15, 1984.

[19] K. Nakayama and K. Wagatsuma, "Weight-based synthesized standards preparation for correction-free calibration in X-ray fluorescence determination of tungsten in high-speed steel," *Analytical Sciences*, vol. 31, no. 8, pp. 851–854, 2015.

[20] M. A. Sperança, P. A. M. Nascimento, and F. M. V. Pereira, "Impurity in sugarcane juice as mineral content: a prospect for analysis using energy-dispersive X-ray fluorescence (EDXRF) and chemometrics," *Microchemical Journal*, vol. 164, Article ID 105951, 2021.

[21] V. Hodges Kip, E. Bleacher Jacob, E. Young Kelsey, and C. A. Evans, "A review of the handheld X-ray fluorescence spectrometer as a tool for field geologic investigations on earth and in planetary surface exploration," *Applied Geochemistry:*, vol. 72, pp. 77–87, 2016.

[22] L. D. Yarbrough, R. Carr, and N. Lentz, "X-ray fluorescence analysis of the bakken and three forks formations and logging applications," *Journal of Petroleum Science and Engineering*, vol. 172, pp. 764–775, 2019.

[23] M. N. Brian, F. Nathan, B. Ron, and G. J. Bruce, "Lithological discrimination of altered volcanic rocks based on systematic portable X-ray fluorescence analysis of drill core at the Myra falls VHMS deposit, Canada," *Journal of Geochemical Exploration*, vol. 193, pp. 1–21, 2018.

[24] J. Shi, Z. Jin, Q. Liu, Z. Huang, and Y. Hao, "Terrestrial sedimentary responses to astronomically forced climate changes during the early Paleogene in the Bohai Bay basin,

eastern China," *Palaeogeography, Palaeoclimatology, Palae-oecology*, vol. 502, pp. 1–12, 2018.

[25] D. J. Kalnicky and R. Singhvi, "Field portable XRF analysis of environmental samples," *Journal of Hazardous Materials*, vol. 83, no. 1-2, pp. 93–122, 2001.

[26] D. E. van Loggerenberg, P. N. Laver, J. G. Myburgh, and C. J. Botha, "Diagnostic value of energy dispersive hand-held X-ray fluorescence spectrometry in determining trace element concentrations in ovine liver," *Biological Trace Element Research*, vol. 190, no. 2, pp. 358–361, 2019.

[27] B. De Samber, G. Silversmit, K. De Schamphelaere et al., "Element-to-tissue correlation in biological samples determined by three-dimensional X-ray imaging methods," *Journal of Analytical Atomic Spectrometry*, vol. 25, no. 4, p. 544, 2010.

[28] L. Perneczky, M. Rauwolf, D. Ingerle et al., "Temporary implementation and testing of a confocal SR-μXRF system for bone analysis at the X-ray fluorescence beamline at elettra," *Nuclear Instruments and Methods in Physics Research Section A: Accelerators, Spectrometers, Detectors and Associated Equipment*, vol. 897, pp. 114–119, 2018.

[29] V. G. Mihucz, G. Silversmit, I. Szalóki et al., "Removal of some elements from washed and cooked rice studied by inductively coupled plasma mass spectrometry and synchrotron based confocal micro-X-ray fluorescence," *Food Chemistry*, vol. 121, no. 1, pp. 290–297, 2010.

[30] S. Schmitz, F. E. Brenker, T. Schoonjans et al., "In situ identification of a CAI candidate in 81P/wild 2 cometary dust by confocal high resolution synchrotron X-ray fluorescence," *Geochimica et Cosmochimica Acta*, vol. 73, no. 18, pp. 5483–5492, 2009.

[31] N. G. Paltridge, P. J. Milham, J. I. Ortiz-Monasterio et al., "Energy-dispersive X-ray fluorescence spectrometry as a tool for zinc, iron and selenium analysis in whole grain wheat," *Plant and Soil*, vol. 361, no. 1-2, pp. 261–269, 2012.

[32] A. Yamauchi, M. Iwasaki, K. Hayashi, and K. Tsuji, "Evaluation of full-field energy dispersive X-ray fluorescence imaging apparatus and super resolution analysis with compressed sensing technique," *X-Ray Spectrometry*, vol. 48, no. 6, pp. 644–650, 2019.

[33] J. S. Almeida, L. A. Meira, M. S. Oliveira, and L. S. G. Teixeira, "Direct multielement determination of Cd, Pb, Fe, and Mn in ground coffee samples using energy dispersive X-ray fluorescence spectrometry," *X-Ray Spectrometry*, vol. 50, no. 1, pp. 2–8, 2021.